Electronic Supplementary Material (ESI) for Nanoscale.

Figure S1. SEM images of PMMA template with different diameters (a) 200 nm, (b) 400 nm. (c) and (d) cross-sectional image of M200-Carbon at low magnification, (e,f) the AFM image of M200-Carbon.

The AFM shows the 3D ordered porous structure of M200, and the diameter of the pores are about 200 nm but the depth of pores are about 400 nm, indicating the pores are connected in the vertical direction after calculation.

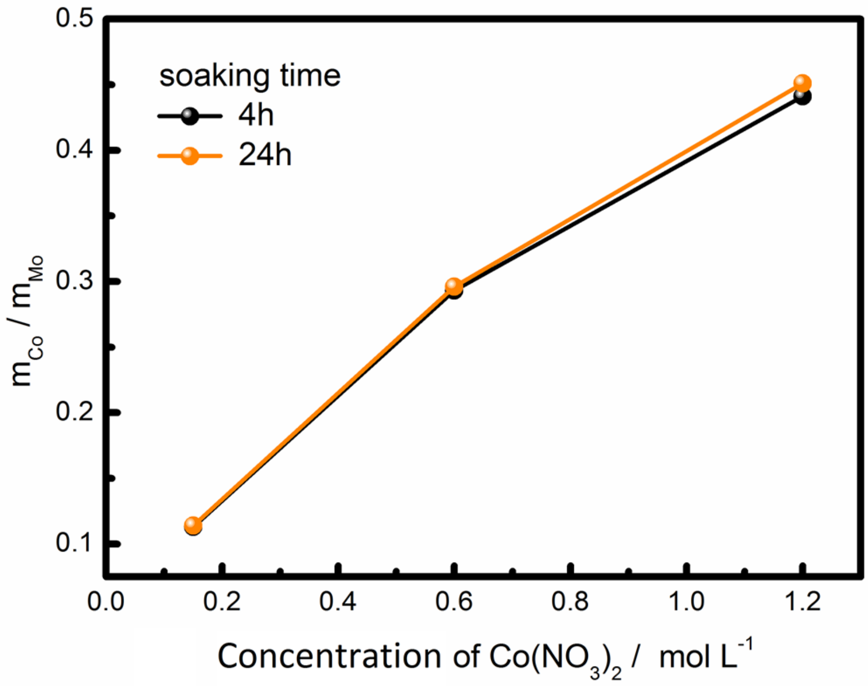

Figure S2. The relationship between the content of Co in the sample (MoO2-CoO-Carbon) and the concentration of $Co(NO_3)_2$ solution.

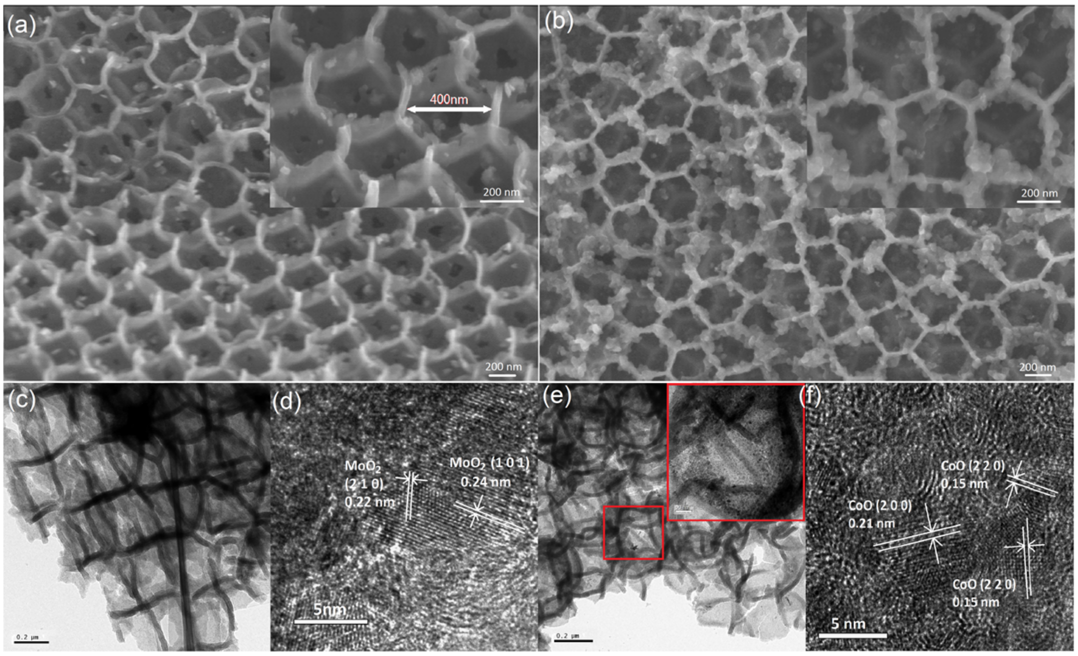

Figure S3. SEM and TEM images of M400-Carbon before (a,c,d) and after CoO modification (b,e,f).

Figure S4. EDS elemental mapping images from TEM for the samples of M400-C-Carbon.

Figure S5. High-resolution XPS spectrum of the Mo 3d (a), C 1s (b), O 1s (c) core level for the sample of M200-Carbon.

Figure S6. (a) XRD spectra of of $MoCl_5$ precursors after oxidation and as-synthesized MoO_3, (b) SEM images of as-synthesized MoO_3.

After calcination in air, the diffraction peaks can be readily indexed to be orthorhombic MoO_3 (Figure S6a), and the morphology of as-synthesized MoO_3 was characterized by SEM in Figure S6b. The red line in Figure S6a is the XRD pattern of $MoCl_5$ precursors after oxidation in air for 24 h, two broad peaks of which located at 12.8° and 27.3° are indexed to MoO_3 in all probability. The as-formed MoO_3 shows not porous but plate-like structure with thickness of about 700 nm.

Figure S7. The CoO disordered porous structures were prepared by the same method as M200-Carbon, as shown in (a), (b) Experimental linear sweep voltammetry curves of the samples (M200-Carbon, M200-C-Carbon, M400-Carbon, M400-C-Carbon) in 1M KOH. (c)Tafel plots of M400-Carbon and M400-C-Carbon at low and high potential region (scan rate 0.5 mV s^{-1}). (d) EIS of M400-Carbon and M400-C-Carbon (e) chronopotentiometry curves of M400-Carbon, M400-C-Carbon on Ni foam electrode under high current densities of 10 and 20 mA cm^{-2}.

Table S1. A detailed comparison of different highly active OER catalysts with various electrode configurations

catalysts	Onset potential / V vs RHE	References
$Zn_xCo_{3-x}O_4$ nanowire arrays grown on Ti foils	1.55 V, pH 14	[1]
$Ni_xCo_{3-x}O_4$ nanowire arrays grown on Ti foils	1.60 V, pH 14	[2]
Ni-substituted Co_3O_4 nanowire arrays grown on Ni foams	1.60 V, pH 14	[3]
Au@Co_3O_4 catalyst	1.58 V, PH 13	[4]

Co_3O_4 nanoparticles grown on reduced oxidized graphene (Co_3O_4/rmGO)	1.54V PH 13	[5]
$Fe_2(MoO_4)_3$ grown on Ni foams	1.51 V, pH 14	[6]

Table S2. Onset potentials, potential at 10 mA cm^{-2}, Tafel slopes at low and high potential regions, charge-transfer resistance for various catalysts

	Onset potential/ V vs RHE	potential at 10 mA cm^{-2} / V vs RHE	Tafel Slope / mV dec^{-1}(high)	Tafel Slope / mV dec-1(low)	charge-transfer resistance Rc t/ Ω
M200-Carbon	1.521	1.549	57.82	210.3	2.818
M200-C-Carbon	1.479	1.502	36.79	116.0	0.4915
M400-Carbon	1.529	1.565	62.73	185.4	34.92
M400-C-Carbon	1.512	1.541	47.39	92.45	4.212

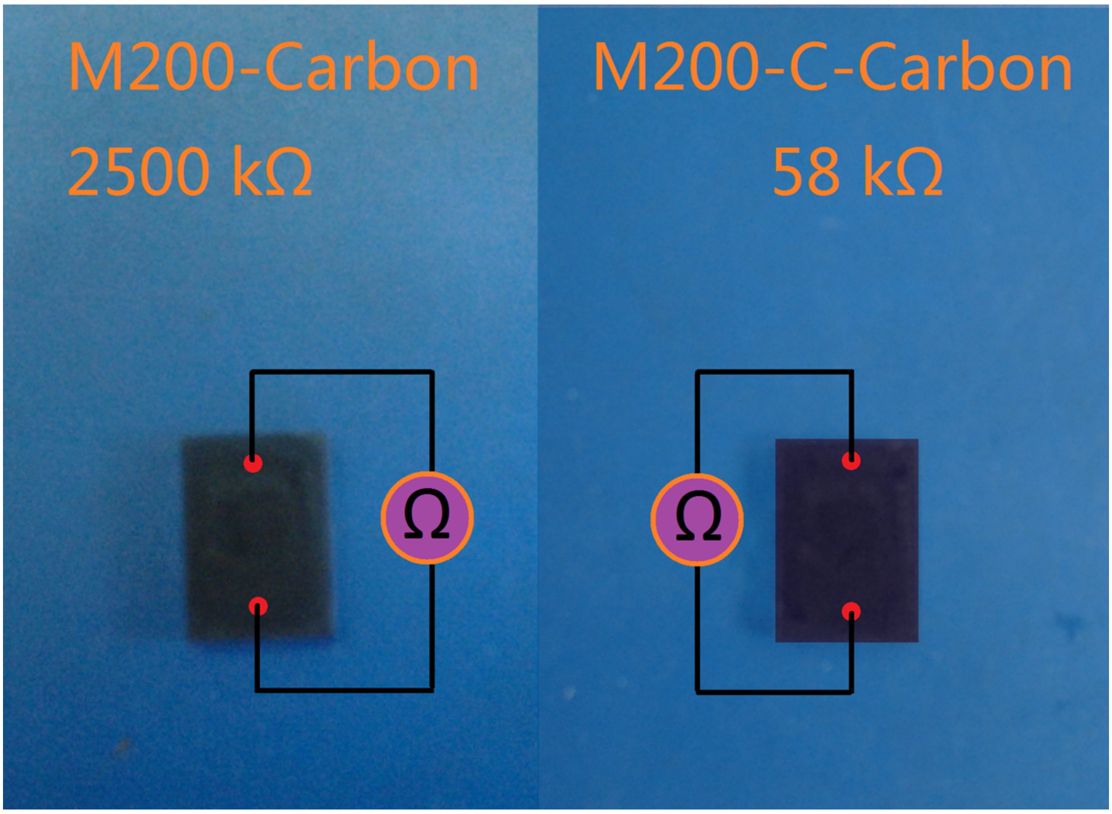

Figure S8. The same amount of two kinds of sample were pasted on the conductive glass uniformly, and the resistance of the two end points can be obtained.

Figure S9. Capacitance measurements and relative comparison of active surface area. (a,b) Cyclic voltammetry curves of M200-Carbon and M200-C-Carbon in the region of 1.0-1.2 V vs. RHE. (c) The differences in current density variation ($\Delta J = J_a - J_c$) at an overpotential of 1.15 V plotted against scan rate fitted to a linear regression enables the estimation of C_{dl}.

The estimation of the effective active surface area of the samples was carried out according to literature. [7] Cyclic voltammetry (CV) were performed at various scan rates (10, 25, 50mV s-1, etc.) in 1.0–1.2 V vs. RHE region. The double-layer capacitance (C_{dl}) of various samples can be determined from the cyclic voltammograms, which is expected to be linearly proportional to the effective surface area (Figure S8 a,b). The exact determination of the surface area is difficult due to the unknown capacitive behavior, but we can safely estimate the relative surface areas. CV measurements were taking in the region of 1.0-1.2 V vs. RHE, which could be mostly considered as the double-layer capacitive behavior. The double-layer capacitance is estimated by plotting the ΔJ (J_a-J_c) at 1.15 V vs. RHE against the scan rate. Analysis shows M200-C-Carbon has a much larger double-layer capacitance than tM200-Carbon. Since the C_{dl} is proportional to the surface area and the conductivity of the materials, more effective active sites can be exposed for M200-C-Carbon, which is responsible for the excellent OER activity.

Figure S10. (a) The typical nitrogen adsorption–desorption isotherm and (b) BJH pore-size distribution plots of M200-Carbon, M200-C-Carbon, M400-Carbon, M400-C-Carbon.

To investigate the specific surface area of samples and pore distribution in the as-prepared samples, N_2 adsorption tests were carried out. Figure S10 shows the nitrogen physisorption isotherms and the corresponding pore size distribution of the samples. All of the samples display a type Ⅱ isotherm with type-H3 hysteresis as defined by IUPAC conventions. Moreover, a significant increase in nitrogen adsorption can be observed at the relative pressure beyond 0.8. The low-pressure portion of the almost linear middle section of the two isotherms suggests that the samples were macroporous adsorbents. However, the small H2 type hysteresis loop in the P/P_0 range of 0.2–0.8, which is related to thae capillary condensation taking place in mesopores, indicates that textural mesopores exist within the wall structure. The pore size distribution curves in Figure S10b also prove that all samples exhibit characteristic pores in a mesopore range. The BET surface area of them were determined, to be (130.6 m^2/g) for M200-Carbon, (71.1 m^2/g) for M200-C-Carbon, (46.3 m^2/g) for M400-Carbon, (43.0 m^2/g) for M400-C-Carbon. Apparently, the BET surface area increases with the the pore size decreasing. On the other side, the addition of cobalt oxide particles will also reduce the BET surface area.

Figure S11. Adsorption behavior curves over MB in darkness of M200-Carbon, M200-C-Carbon, M400-Carbon, M400-C-Carbon.

In order to evaluate the specific surface area of these porous structures in liquid phase without the drying, thermal annealing and vacuum degassing processes, MB ethanol solution method was used to characterize the MB absorption on the 3DOM structures (Figure S11). Figure S11e shows their adsorption behaviors over MB in darkness. It can be found that the 3DOM M200-Carbon exhibit stronger adsorption properties than that of M400-Carbon during the adsorption time of 60 min. This is partially due to the non-covalent intermolecular π–π interactions between pollutant molecules and the carbon skeleton. [8,9] After CoO modification, the adsorption behaviors decrease, which may be because the inner surface of carbon skeleton was covered by CoO nanoparticles, reduces attractive forces between the negative carbon and the positively charged MB molecules. This result is consistent with the N_2 adsorption tests. The larger surface area serves more reaction interfaces, which are beneficial to enhance OER property. And the addition of CoO particles also provides more active sites, which are beneficial to obtain the higher OER activity.

Figure 12. (a) CV tests of M200-Carbon and M200-C-Carbon conducted in N_2 and O_2 saturated 1M KOH aqueous solution, (b) LSVs of M200-Carbon and M200-C-Carbon at 400 - 2025 rpm, (c)K-L plots of M200-Carbon and M200-C-Carbon at different potentials vs RHE, (d) Chronoamperometric responses of M200-C-Carbon at 0.5 V vs RHE in 1M KOH solution without methanol (0-2 h) and with adding methanol (2-4 h).

In order to identify the activity trend in ORR is opposite to OER or not, it is worthy to investigate the ORR activity of M200-Carbon before and after CoO modification. To study the ORR catalytic activity, the as-prepared catalysts were first loaded onto glassy carbon electrodes to investigate the cyclic voltammetry (CV) behavior in a 1 M KOH electrolyte by using a three-electrode system. Figure S12a shows the CV curves of M200-C-Carbon and M200-Carbon in O_2 versus N_2-saturated electrolytes, and all data were recorded by cycling the potential at a scan rate of 10 mV s^{-1} until reproducible CVs were obtained. In comparison with the electrochemical response in N_2-saturated electrolyte, both M200-Carbon display an apparent cathodic peak, which is attributed to the electrocatalytic reduction of oxygen on the electrode. Morover, upon functionalization of the M200-Carbon with CoO, both the onset potential and the reduction peak potential of ORR shifted positively.The rotating disk electrode (RDE) measurements were performed to investigate the electrochemical kinetics of M200-C-Carbon and M200-Carbon in ORR. To further investigate the ORR performance, we carried out the linear sweep voltammetry (LSV) measurements on a rotating disk electrode (RDE) for each of the electrode materials, including M200-Carbon and M200-C-Carbon, in O_2-saturated 1 M KOH at a scan rate of 10 mV s^{-1} (Figure S12b)

The ORR mechanism was examined with the Koutecky-Levich correlations by using the following equations [10-12]:

$$\frac{1}{I_d} = \frac{1}{I_k} + \frac{1}{I_{dl}} = \frac{1}{I_k} + \frac{1}{B}\omega^{-1/2}$$

$$B = 0.62nFC_{O_2}D_{O2}^{2/3}\mathrm{v}^{-1/5}$$

In these equations, Id, Ik and Idl are the disk current density, the kinetic current density and the diffusion limiting current density, respectively. Moreover, n is the electron transfer number, F is the Faraday constant (96,485 C mol^{-1}), C_{O2} is the concentration of O_2 in KOH solution (1.14×10^{-6} mol cm^{-3}), D_{O2} is the oxygen diffusion coefficient in KOH (1.73×10^{-5} cm^2 s^{-1}) and n is the kinematic viscosity of the KOH solution (0.01 cm^2 s^{-1}), ω is the electrode rotation rate (rpm). So there should be a linear relationship between $1/I_d$ and $\omega^{-1/2}$, the intercept is equal to $1/I_k$, and the number of the electrons transferred during the reaction could be calculated from the slope.

Based on the slopes of the Koutecky–Levich plots (Figure S12), the electron transfer number (n) was calculated as 0.8 and 1.7 at 0.4–0.6 V for M200-Carbon and

M200-C-Carbon, respectively. The electron transfer number of M200-Carbon suggests that the ORR are negligible. After CoO modification, the M200-Carbon–CoO involves a two-step reduction process with H_2O_2 as the intermediate agent. To understand the fundamental steps of ORR on M200-C-Carbon, the standard ORR processes in alkaline solutions via a 2e$^-$ are as follows:

O_2 (M200-C-Carbon)+H_2O+2e$^-$ → HO^{2-}(M200-C-Carbon)+OH$^-$ (1)

HO_2^-(M200-C-Carbon)+H_2O+2e$^-$ → 3OH$^-$(M200-C-Carbon) (2)

When a certain amount of electrons is introduced (e.g., two electrons in our reaction), the free energy of intermediate OOH@(M200-C-Carbon) decreases to a comparable level with that of the initial state of O_2@(M200-C-Carbon), indicating that the first 2e$^-$ reaction (eq 1) can spontaneously proceed. However an obvious barrier still exists at the final state of OH$^-$(M200-C-Carbon), which then blocks the occurrence of the second 2e$^-$ reaction (eq 2). As a result, a lot of adsorbed OOH$^-$ intermediate products accumulate on M200-C-Carbon, causing a significant ORR resistance. Therefore, the activity trend of M200-C-Carbon in ORR is not opposite to OER in present work. Remarkably, as shown in Figure 3d, the original cathodic ORR current of M200-C-Carbon under 0.5 V did not show a significant change after the scheduled sequential addition of methanol into the electrolyte solution, which indicates M200-C-Carbon has good methanol tolerance ability for cathode materials in low-temperature fuel cells.

Figure S13. (a-d) Cyclic voltammetry curves of M200-Carbon, M200-C-Carbon, M400-Carbon and M400-C-Carbon in the region of 0.5 - 2.1 V vs RHE in 1 M KOH solution, (e) the dependence of the peak current (Ip) on the square root of the scan rate

The electroactive surface areas of the the catalyst series were estimated by the cyclic voltammetry method. Under the temperature of 25 °C, the dependence of the peak current on the square root of the scan rate was described by the Randles–Sevcik equation:

$$\mathrm{Ip} = 0.04463(\mathrm{F}^3/\mathrm{RT})^{1/2}\mathrm{n}^{3/2}\mathrm{AD}_0^{1/2}\mathrm{C}_0\mathrm{v}^{1/2} \tag{3}$$

Where n represents the number of electrons participating in the redox reaction, ν was the scan rate (mV s^{-1}), mA was the electroactive area of the electrode (cm^2), D_0 was the diffusion coefficient the diffusion coefficient of 1 M KOH, C_0 was the concentration of the probe molecule in the bulk solution (mol cm^{-3}), (here, we denote the Ni redox peaks as the probe signal). And Ip was the redox peak current (mA) illustrated in CV curves. For T=298 K (25 °C); $0.4463(F^3/RT)^{1/2}=2.687\times10^5$(mol $V^{1/2}$). Therefore, the value of $[0.4463(F^3/RT)^{1/2}n^{3/2}AD_0{}^{1/2}C_0]$ is a constant, which correspongding to the slope in Figure S13e.

References

[1] X. J. Liu, Z. Chang, L. Luo, T. H. Xu, X. D. Lei, J. F. Liu, X. M. Sun, Chem. Mater. 2014, 26, 1889 - 1895.

[2] Y. G. Li, P. Hasin, Y. Y. Wu, Adv. Mater. 2010, 22, 1926 - 1929.

[3] B. G. Lu, D. X. Cao, P. Wang, G. L. Wang, Y. Y. Gao, Int. J. Hydrogen Energ. 2011, 36, 72 - 78.

[4] Z. B. Zhuang, W. C. Sheng, Y. S. Yan, Adv. Mater. 2014, 26, 3950 – 3955.

[5] Y. Y. Liang, Y. G. Li, H. L. Wang, J. G. Zhou, J. Wang, T. Regier, H. J. Dai, Nat. Mater. 2011, 10, 780 - 786.

[6] V. K. V. P. Srirapu, C. S. Sharma, R. Awasthi, A. S. K. Singh, Phys. Chem. Chem. Phps. 2014, 16, 7385 - 7393.

[7] Lukowski, M. A.; Daniel, A. S.; Meng, F.; Forticaux, A.; Li, L.; Jin, S. J. Am. Chem. Soc. 2013, 135, 10274 10277.

[8] D. F. Xu, B. Cheng, S. W. Cao, J. G. Yu, Appl. Catal. B-Environ. 2015, 164, 380–388.

[9] H. Zhang, X. J. Lv, Y. M. Li, Y. Wang, J. H. Li, ACS Nano 2010, 4, 380 - 386.

[10] C. Jin, X. Cao, L. Zhang, C. Zhang, R. Yang, J. Power Sours. 2013, 241, 225 – 230.

[11] M. Thommes, Chemie Ingenieur Technik 2010, 82, 1059 – 1073.

[12] K. E. Gubbins, R. D. Walker, J. Electrochem. Soc. 1965, 112, 469 – 471.